Study of the influence of interfacial waves on heat transfer in turbulent falling films

Nikhin Mascarenhas, Issam Mudawar *

Purdue University Boiling and Two-Phase Flow Laboratory (PU-BTPFL), School of Mechanical Engineering, 585 Purdue Mall, West Lafayette, IN 47907, USA

ABSTRACT

This study explores the influence of interfacial waves on mass, momentum and heat transfer in turbulent, free-falling water films that are subjected to sensible heating. Measured temporal records of film thickness and temperature profile across the film are used to examine the film's thermal response to the passage of large waves. The temporal variations of liquid temperature and heat transfer coefficient are generally opposite to that of film thickness; the heat transfer coefficient is highest in the substrate regions upstream and downstream of large waves and lowest in the waves themselves. Increasing the film's Reynolds number increases the mean thickness and wave amplitude, and decreases the wave period, but results in appreciable attenuation in the measured liquid temperature response to the large waves. Using FLUENT, a computational model of the falling film is constructed and its predictions compared to the data. The computed results show good agreement with the measured mean film thickness, wave form and period, and both wall and mean film temperatures. The model captures the measured increase in liquid temperature in the film substrate and decrease corresponding to the large waves, but the predicted temperature response is less attenuated for higher Reynolds numbers than the measured. Velocity predictions point to acceleration of high temperature liquid from the upstream substrate toward the cold region within the large wave before losing the excess heat due to mixing downstream from the wave crest. Overall, the present study demonstrates the effectiveness of computational tools at predicting the hydrodynamic and thermal characteristics of separated flows involving a wavy liquid–vapor interface.

© 2013 Elsevier Ltd. All rights reserved.

1. Introduction

The ability to deliver high heat transfer coefficients is a primary reason behind the popularity of liquid–vapor systems in a broad range of application. But a key drawback to many of these systems is high pressure drop, which has negative implications to system efficiency. This explains the popularity of liquid–vapor systems that rely mostly on gravity to achieve fluid motion, and, therefore, operate with minimal pressure drop penalty. These include pool boiling thermosyphons [1,2] and pumpless gravity driven loops [3,4].

Free-falling liquid films constitute another category of liquid–vapor systems that rely on gravity to achieve fluid motion. They provide impressive heat transfer performance by (i) minimizing conduction resistance across the film (especially for thin, laminar films), (ii) capitalizing upon turbulent eddies (especially for high liquid flow rates), and (iii) taking advantage of the added mixing provided by interfacial waves. These attributes explain the popularity of free-falling films in numerous thermal systems, including

condensers, evaporators, spray-type refrigerators, distillation columns, chemical reactors, and nuclear reactors.

But despite their seemingly simple separated flow structure compared to internal liquid–vapor flows, falling films are complicated by (i) dampening of turbulent eddies at the film interface due to surface tension, (ii) difficulty ascertaining transition from laminar to turbulent flow, and (iii) highly complex influence of interfacial waves on the film's mass, momentum and heat transport. Furthermore, these influences are interdependent on one another.

1.1. Interfacial characteristics of falling films

Interfacial waves enhance the transport behavior of films by increasing interfacial area, reducing mean film thickness, and intensifying turbulence, and these influences are highly dependent on the film's Reynolds number ($Re = 4\Gamma/\mu$). Although waves are viewed as mostly stochastic, prior studies have provided very useful insight into the film's interfacial behavior. Waves are absent only for very low Reynolds number *smooth-laminar* films, such as those examined by Nusselt in his pioneering study of film condensation [5]. Kapitza [6] showed that waves that form on predominantly laminar films are

* Corresponding author. Tel.: +1 765 494 5705; fax: +1 765 494 0539.
E-mail address: mudawar@ecn.purdue.edu (I. Mudawar).

Nomenclature

C_μ	turbulence model constant
D_H	hydraulic diameter
$e_{i,j}$	strain rate tensor
g	gravitational acceleration
h_H	heat transfer coefficient for sensible heating $q''_w/(T_w - T_m)$
k	thermal conductivity; turbulent kinetic energy
n_j	unit normal vector on free interface
P	pressure
Pr	Prandtl number
Pr_t	turbulent Prandtl number
q''_w	wall heat flux
r	radial coordinate
Re	Reynolds number
R_1, R_2	radii of curvature at free interface
s_{ij}	fluctuating component of strain rate tensor
t	time
T	temperature
t_i	unit tangential vector on free interface
T_m	mean film temperature
u	velocity
U	inlet streamwise velocity
u_r	r-direction velocity component
u_x	x-direction velocity component
V	inlet normal velocity
x	axial coordinate
y	coordinate perpendicular to the wall

Greek symbols

α	thermal diffusivity
Γ	film mass flow rate per unit film width
δ	film thickness
ε	dissipation rate of turbulent kinetic energy
μ	dynamic viscosity
v	kinematic viscosity
ρ	density
σ	surface tension

Subscripts

f	fluid
i	direction index; film interface
in	inlet
j	direction index
m	mean
s	solid
t	turbulent
w	wall
Γ	solid-liquid interface

Superscripts

$-$	average component
$+$	non-dimensionalized
$'$	fluctuating component

a combination of short, near-sinusoidal capillary waves and a few long, near-solitary waves. Similar observations of *wavy-laminar* films were reported by Adomeit and Renz [7], who measured wave characteristics for $27 < Re < 200$. Chu and Dukler [8] shifted focus to moderate Reynolds numbers in the range of $300 < Re < 1,000$. They found long waves to increase in frequency, accompanied by formation of shorter waves that were generated by vortex shedding of the long waves.

Several studies have shown that wave structure for high Reynolds number *turbulent films* is fundamentally different from that observed at low and moderate Re. Here, the film features predominantly long waves that are strongly influenced by turbulence within the film and travel at speeds considerably larger than the mean film speed, and increase in amplitude with increasing Re [9–11]. Employing a wire conductance technique to amass temporal records of film thickness for moderate to high Reynolds numbers ($509 < Re < 13,090$), Karapantsios *et al.* [12] showed that waves on turbulent films are highly stochastic, but the increase in amplitude of large waves with increasing Reynolds number ceases for $Re > 5,000$, which contributes to substrate thickening for high Re turbulent films.

To assess the influence of interfacial waves on velocity and turbulence within turbulent free-falling liquid films, Mudawar and Houpt [13,14] performed detailed measurements of interfacial waves on free-falling water-propylene glycol films simultaneously with laser-Doppler velocimeter measurements within the film. They showed that large waves behave as lumps of liquid sliding over a continuous substrate. Temporal changes in stream-wise velocity were found to resemble but slightly lag those of film thickness. Furthermore, large waves were determined to play a significant role in transporting the film's mass, carrying 40-70% of the total mass flow rate.

1.2. Experimental falling-film thermal transport studies

Earlier experimental studies on free-falling turbulent liquid films that are subjected to heating were focused mostly on development of correlations for time-averaged film thickness and heat transfer coefficient. These include the works of Wilke [15], Gimbutis [16], Ganchev et al. [17], and Shmerler and Mudawar [18,19]. Lyu and Mudawar [20–22] performed similar experiments but with particular emphasis on the statistical characteristics of the interfacial waves, and temporal variations of temperature profile across the film and heat transfer coefficient. They found liquid temperature at a fixed distance from the wall to increase in the thin substrate portion of the film and decrease within the large waves. This caused large fluctuations in the heat transfer coefficient in response to the passage of large waves.

1.3. Computational modeling of liquid films

FLUENT has become a popular tool over the past decade to predict liquid film hydrodynamics. Using FLUENT with the Volume of Fluid (VOF) Model, Gu et al. [23] simulated adiabatic liquid film flow on an inclined wall, and identified a variety of flow patterns for different film thicknesses. Jafar et al. [24] used FLUENT to study film thickness and flow mode variations for turbulent films falling on horizontal cylinders with Reynolds numbers as high as 3,200. Xu et al. [25] simulated mass transfer across low Reynolds number falling films and predicted instantaneous concentration profiles and corresponding mass transfer rates. Bo et al. [26] employed FLUENT to predict temperature and concentration profiles in a counter-flow absorber that agreed well with published models. The VOF Model was used by Ho et al. [27] to predict liquid film thickness as well as velocity, pressure and shear stress profiles in falling film micro-reactors. Recently, Sun et al. [28] broadened
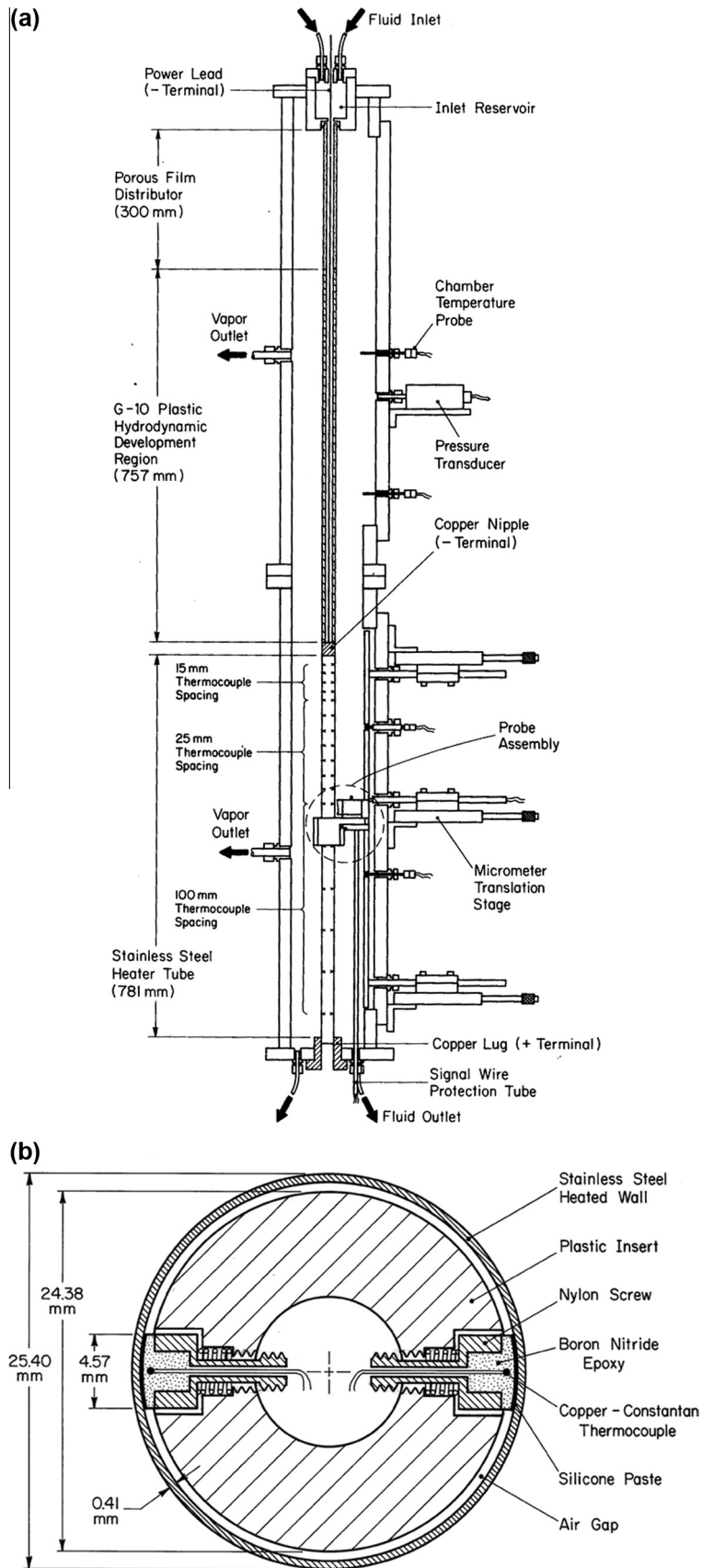
(a)

Fluid Inlet

Power Lead
(– Terminal)

Inlet Reservoir

Porous Film
Distributor
(300 mm)

Vapor
Outlet

Chamber
Temperature
Probe

Pressure
Transducer

G-10 Plastic
Hydrodynamic
Development
Region
(757 mm)

Copper Nipple
(– Terminal)

15 mm
Thermocouple
Spacing

25 mm
Thermocouple
Spacing

Probe
Assembly

Vapor
Outlet

Micrometer
Translation
Stage

100 mm
Thermocouple
Spacing

Stainless Steel
Heater Tube
(781 mm)

Copper Lug (+ Terminal)

Signal Wire
Protection Tube

Fluid Outlet

(b)

Stainless Steel
Heated Wall

Plastic Insert

Nylon Screw

Boron Nitride
Epoxy

Copper – Constantan
Thermocouple

Silicone Paste

Air Gap

24.38
mm

25.40
mm

4.57
mm

0.41
mm

Fig. 1. (a) Cut-away view of test chamber, (b) cross-sectional view of inner thermocouples, (c) schematic diagram of flow loop, (d) photo of test facility.
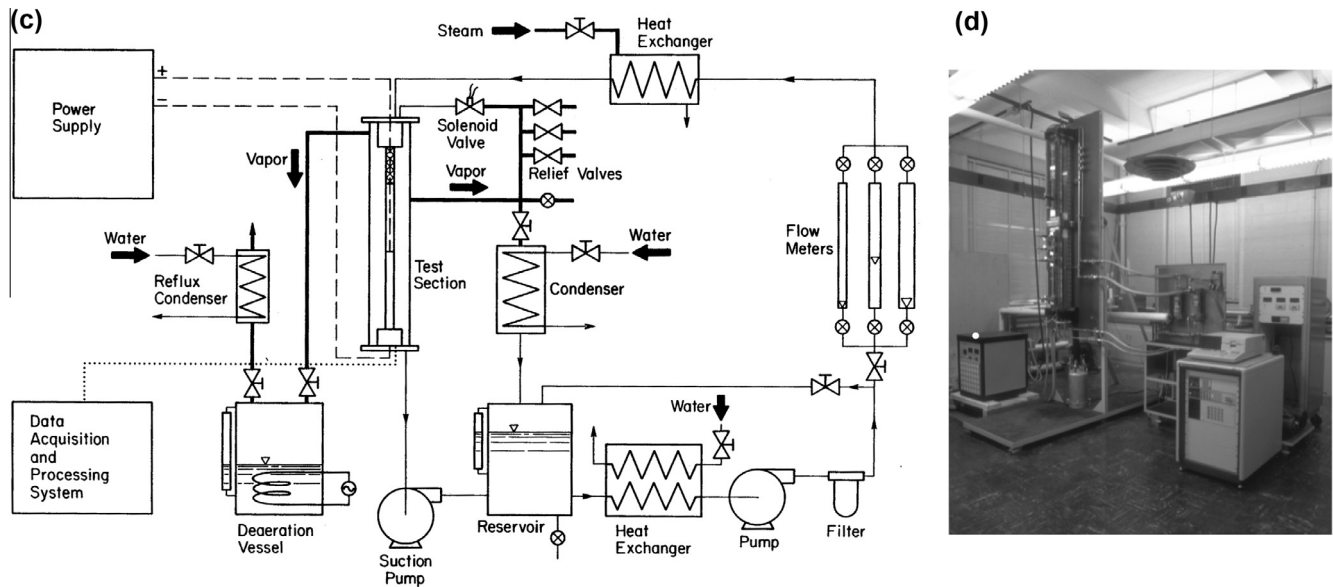
Fig. 1 (*continued*)

the findings of Jafar et al. [24] with more detailed study of film flow characteristics.

Recently, the authors of the present study used FLUENT to explore the interfacial dampening of turbulent eddies for wavy, free-falling turbulent liquid films subjected to sensible heating [29]. Good agreement was achieved between predicted axial variations of the mean heat transfer coefficient and experimental data. It was also shown that turbulent eddies are fully suppressed at the interface, and eddy diffusivity possesses a maximum between the wall and free interface.

The present study is a follow up to [29] concerning turbulent, free-falling liquid films subjected to sensible heating, but with a primary focus on the response of liquid temperature profile and heat transfer coefficient to the passage of large interfacial waves. Using FLUENT, temporal records of film thickness and liquid temperature profile are predicted at different regions of large waves and compared to experimental records. These predictions are used to explain the impact of large waves on the heat transfer coefficient.

2. Experimental methods

This study employs data that are measured using the Purdue University Boiling and Two-Phase Flow Laboratory (PU-BTPFL) falling film facility, which utilizes a number of instrumentation tools to investigate the transport behavior of free-falling liquid films undergoing sensible heating [18,20–22,29], evaporation [19], and boiling [30]. Unlike the instrumentation described recently in [29], which provides time-averaged measurements of wall and mean film temperatures, the instrumentation described here provides a series of simultaneous *instantaneous* measurements of (1) film thickness and wave shape, (2) wave velocity, (3) wall temperature, and (4) temperature profile across the film. The information provided with this instrumentation is used to assess the accuracy of computational predictions for turbulent, free-falling water films subjected to sensible heating.

2.1. Falling-film test section

The main component of the experimental facility is a test chamber, where the falling film is generated. As shown in Fig. 1(a), the

film is gravity-driven on the outside wall of a cylindrical 25.4-mm diameter test section consisting of three parts: a 300-mm polyethylene porous film distributor, a 757-mm long G-10 fiber-glass plastic hydrodynamic development section, and a 781-mm long stainless steel heated section. The film is subjected to uniform wall heat flux along the lower thin-walled stainless steel tube by passing up to 750 A at 15 V from a d.c. power supply.

Thermocouple pairs made from 0.127-mm diameter type-T wire are used to measure the inside wall temperature of the stainless steel tube at 17 axial locations. More thermocouple pairs are concentrated towards the top of the stainless steel tube to capture thermal entrance effects. The pairs are diametrically opposite to aid in vertical alignment of the test section. The falling film is deemed symmetrical when the maximum temperature difference between thermocouples at the same vertical location is less than 0.1 °C. As shown in Fig. 1(b), the bead of each thermocouple is embedded in a small mass of thermally conducting boron nitride epoxy deposited within the head of a 6-32 nylon socket head cap screw. The epoxy is carefully machined to match the cylindrical shape of the stainless steel tube. The screw is maintained in contact with the inner wall of the stainless steel tube with the aid of a stainless steel spring. The screw is inserted radially inwards into an inner thermally insulating tube made from Delrin plastic. During assembly, the screw heads are covered with thermally conducting grease, then the thermocouple pairs are compressed inwards to allow insertion of the Delrin tube through the stainless steel tube.

2.2. Water conditioning loop

Deionized water is deaerated by vigorous boiling before being charged into the flow loop illustrated schematically in Fig. 1(c). The primary purpose of the loop is to deliver the water to the test chamber at the desired flow rate and temperature at near-atmospheric pressure. The water temperature is fine-tuned by regulating steam flow through a heat exchanger located upstream of the test chamber. Electrical power is then supplied to the test section until steady state conditions are achieved both within the film and surrounding vapor.

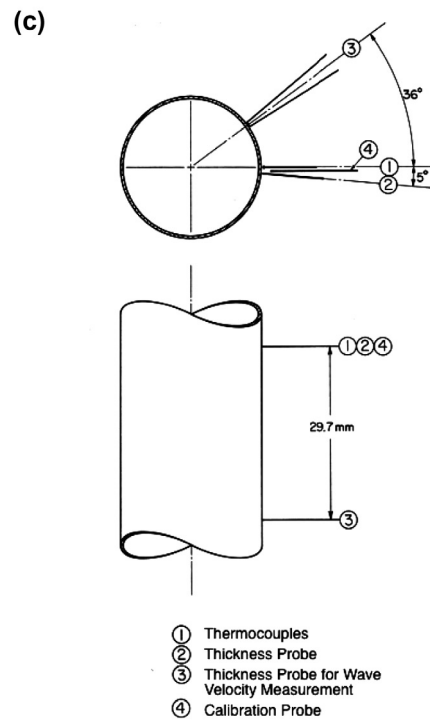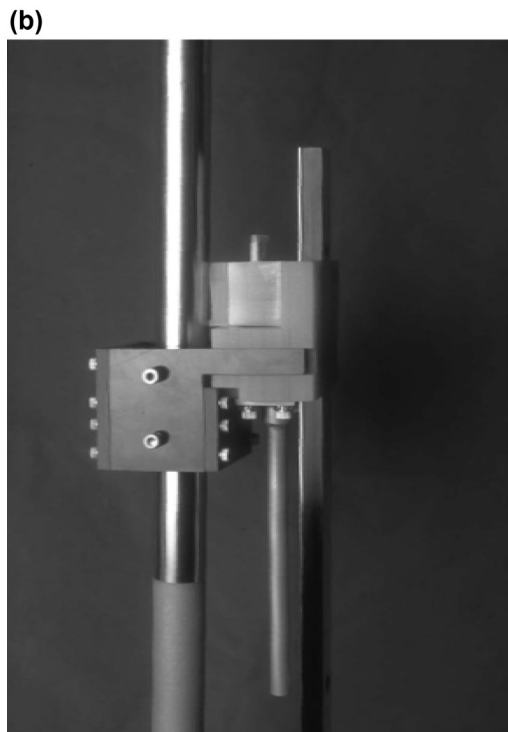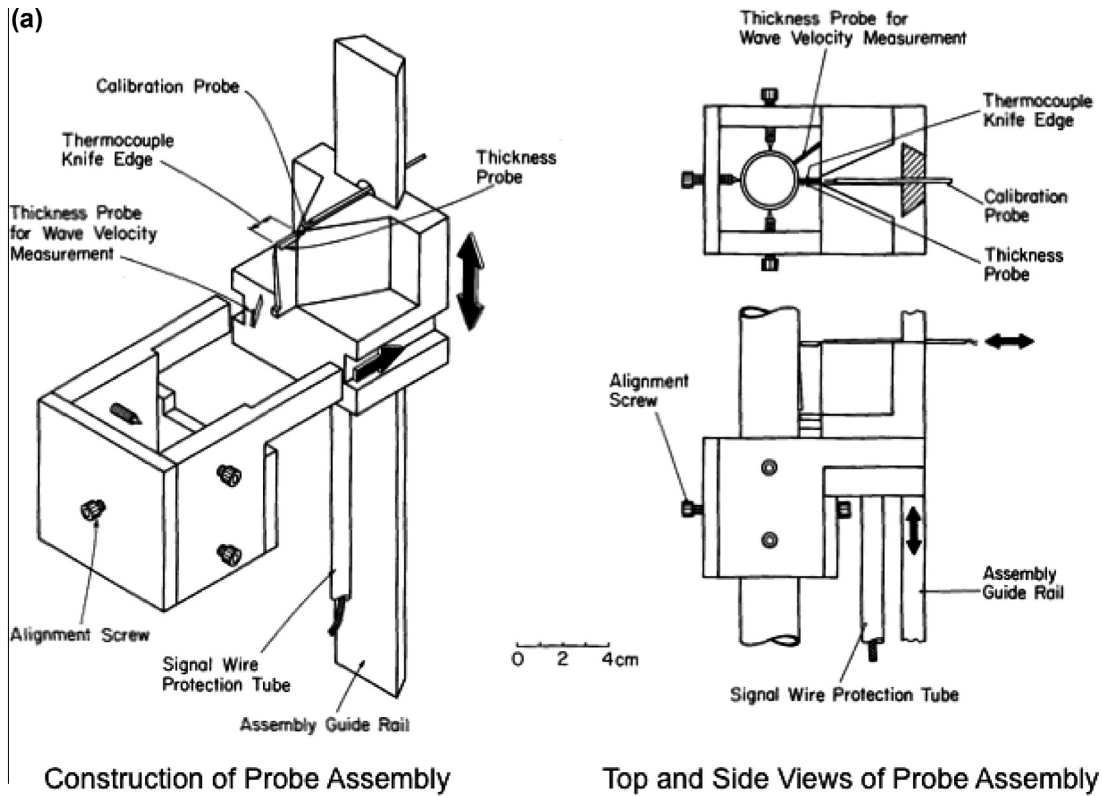Fig. 1(d) shows a photo of the entire test facility, including the test chamber and flow loop.

(a)

Calibration Probe

Thermocouple Knife Edge

Thickness Probe for Wave Velocity Measurement

Thickness Probe

Alignment Screw

Signal Wire Protection Tube

Assembly Guide Rail

0   2   4cm

Construction of Probe Assembly

Thickness Probe for Wave Velocity Measurement

Thermocouple Knife Edge

Calibration Probe

Thickness Probe

Alignment Screw

Assembly Guide Rail

Signal Wire Protection Tube

Top and Side Views of Probe Assembly

(b)

(c)

36°

5°

29.7 mm

① Thermocouples
② Thickness Probe
③ Thickness Probe for Wave Velocity Measurement
④ Calibration Probe

Fig. 2. (a) Construction of probe assembly, (b) photo of probe assembly, (c) relative positions of thickness and temperature probes.

2.3. Falling-film instrumentation

Fig. 2(a) and (b) depict an assembly block that is used to support the delicate liquid film temperature and thickness probes. This block features six alignment screws which help center the block around the stainless steel tube; the screws are situated downstream of the probes to prevent any influence on the film measurements. The instrumentation block is positioned axially with the aid of a vertical guide rail, while horizontal motion is controlled by two micrometer translation stages attached to the guide rail. The film

data presented in this study are measured 278 mm below the top of the stainless steel section, well outside the thermal entrance region.

Fig. 2(c) shows the relative positions of the falling-film instrumentation, which consists of: (1) an array of thermocouples that traverse the film, (2) a thickness probe, (3) a second thickness probe used for wave velocity measurements, and (4) a probe for calibrating the thickness probe. The thermocouple array, thickness probe and thickness calibration probe are all mounted in the same plane, while the second thickness probe is situated 29.7 mm downstream with a 41° azimuthal offset to avoid the wakes created by the upstream probes.

Fig. 3(a) and (b) show the construction of a G-10 fiberglass plastic knife-edge that is used to support twelve thermocouples spanning 5 mm from the stainless steel wall. Notice how more thermocouples are concentrated near the stainless steel wall to help capture the near-wall thermal boundary layer. The thermocouples are made from 0.0506-mm type-E wire with a bead diameter of 0.0762 mm. Close proximity between thermocouples and lead wires require careful assembly under a microscopic lens. This is achieved by, first, positioning the thermocouple bead closest to the heated wall in place and coating its wires on either side of the knife-edge with a thin layer of epoxy. The other thermocouples are sequentially assembled in the same manner in order of distance from the heated wall. Fig. 3(a) shows a contact plane protruding from the downstream side of the knife-edge whose purpose is to protect the instrumented portion of the knife-edge by preventing it from making direct contact with wall.

The thermocouples are calibrated in a constant temperature bath at several temperatures to a standard deviation of 0.17 °C. The probe assembly block is then mounted around the stainless steel tube and the lower portion of the test chamber filled with water with the probe assembly block completely submerged. The d.c. current is then supplied across the stainless steel tube to the same heat flux levels applied during the subsequent falling film experiments to calibrate the thermocouples for the offset resulting from the d.c. current. The calibration procedure is repeated several times after using a batch of deionized water in the falling film configuration to maintain thermocouple offset below 0.2 °C.

Film thickness is measured with the aid of a hot-wire probe made from 0.0254-mm diameter platinum-10% rhodium wire that is extended across the liquid-vapor interface as shown in Fig. 3(c). A constant d.c. current is applied through the probe wire, and film thickness inferred from variations in the probe's voltage drop. This measurement technique is based upon two crucial criteria: large ratio of heat transfer coefficient along the portion of probe wire submerged in liquid compared to that in vapor, and strong relationship between electrical resistance and temperature. With both criteria carefully validated, passage of a constant current through the probe yields a voltage drop that is a function of the length of wire submerged in liquid alone. This probe requires extensive calibration, which is achieved first by submerging the probe vertically downward in a small test cell containing a stagnant layer of water to generate the linear dependence of voltage drop on water layer thickness. In situ calibration is then performed prior to each test at heating conditions identical to those of the test itself using the calibration probe shown in Fig. 3(c). Once the thickness probe is mounted across the film, the calibration probe is translated horizontally towards the film interface. A surge in the calibration probe's signal occurs once the tip of the calibration probe contacts the film interface. A single calibration point is realized by the relationship between voltage drop of the thickness probe and separation distance of the calibration probe at the instant the calibration probe contacts the film interface. This calibration technique is
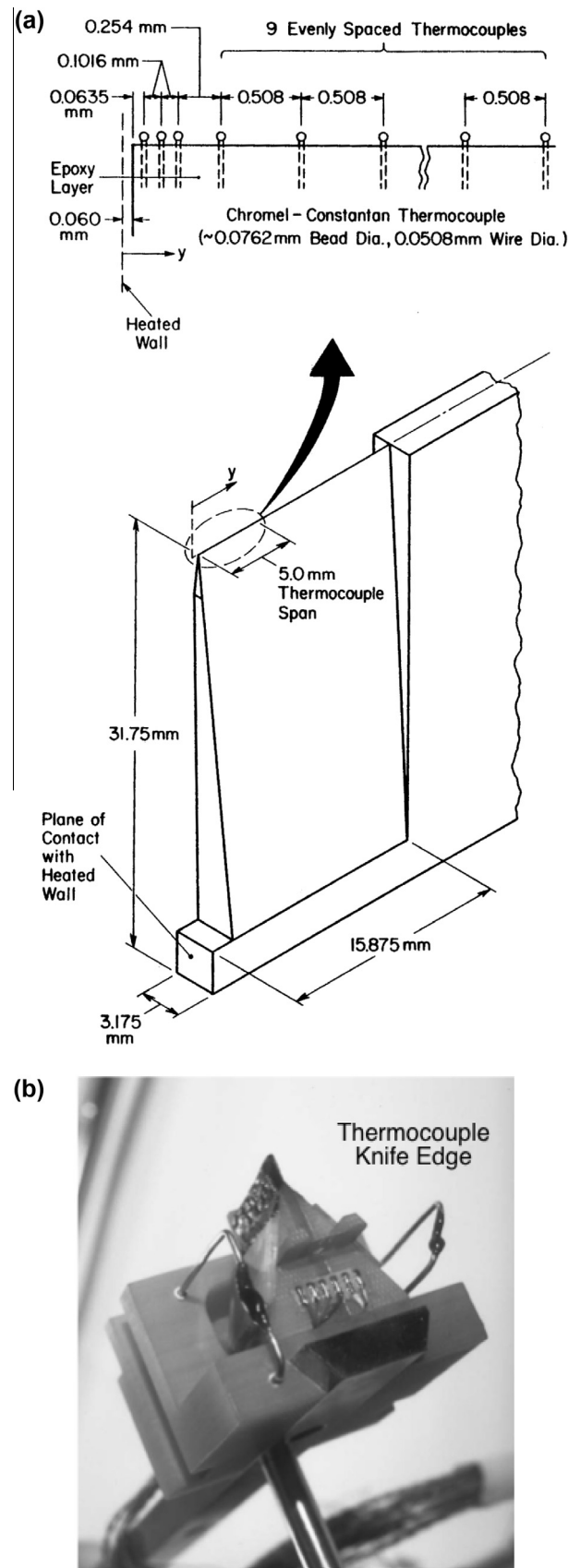

Fig. 3. (a) Construction of thermocouple knife-edge, (b) photo of thermocouple knife-edge on probe assembly, (c) construction of thickness probe and thickness calibration probe.
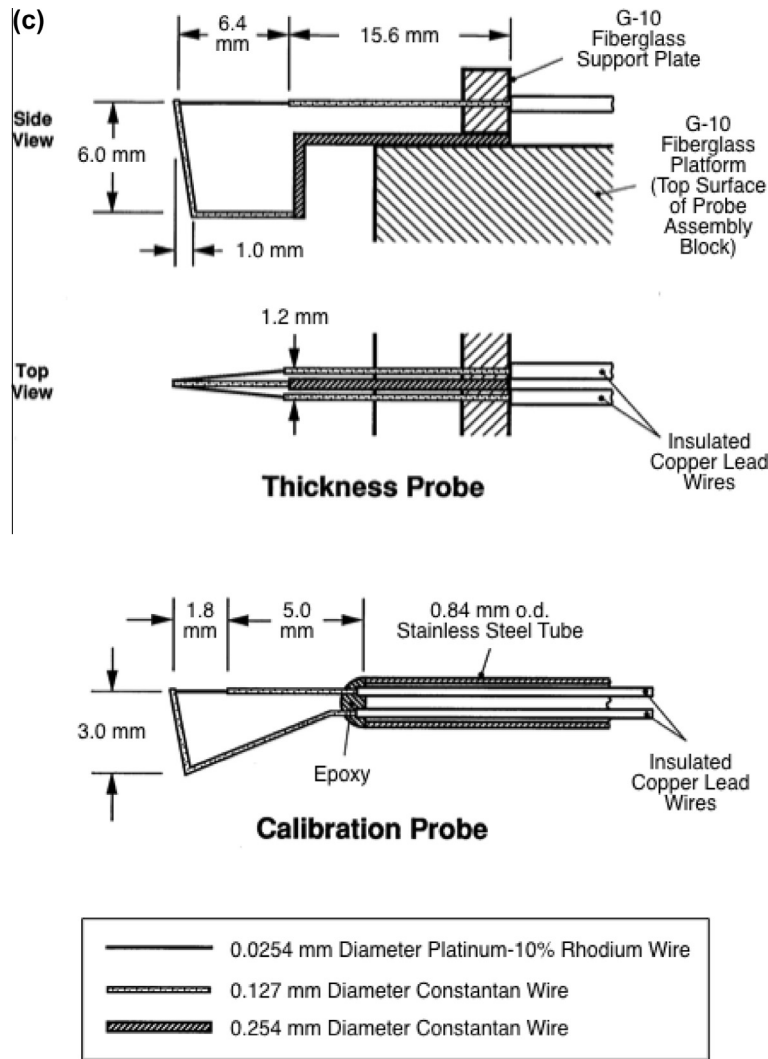
(c)

Side View

6.0 mm

6.4 mm

15.6 mm

1.0 mm

G-10 Fiberglass Support Plate

G-10 Fiberglass Platform (Top Surface of Probe Assembly Block)

Top View

1.2 mm

Thickness Probe

Insulated Copper Lead Wires

1.8 mm

5.0 mm

0.84 mm o.d. Stainless Steel Tube

3.0 mm

Epoxy

Insulated Copper Lead Wires

Calibration Probe

———	0.0254 mm Diameter Platinum-10% Rhodium Wire
-----------	0.127 mm Diameter Constantan Wire
/////////	0.254 mm Diameter Constantan Wire

Fig. 3 (*continued*)

repeated by translating the calibration probe to other positions closer to the heated wall. The measurement resolution and response time of the thickness probe are ascertained at 0.05 mm and 0.14 ms, respectively [22].

Temperature profile across the film is measured simultaneously with the film thickness over a sampling period of 1 s at a frequency of 500 Hz. The temperature data are processed by low pass filtering the temporal records using a fourth order, 0.1 dB Chebyshev digital filter code written by Walraven [31]. External noise is eliminated by a 100 Hz low pass filter to avoid influencing the temperature data.

3. Numerical methods

Fig. 4 describes the computational domain used in the present simulation. The flow is assumed two-dimensional and axisymmetric, given the cylindrical construction of the test section and small ratio of film thickness to distance between the test section and test chamber walls. The simulated system consists of the inlet reservoir, porous film distributor and 1,835-mm long annulus formed between the outer wall of the 25.4-mm diameter test section and test chamber walls. The annulus of the computational domain is assigned an outer radius based on an annular area equal to actual area between the test section and test chamber's inner walls.
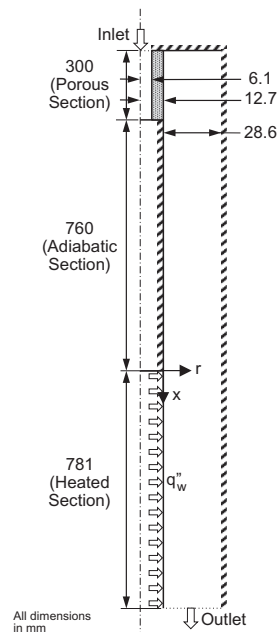
Inlet

300 (Porous Section)

6.1

12.7

28.6

760 (Adiabatic Section)

781 (Heated Section)

r

x

q''_w

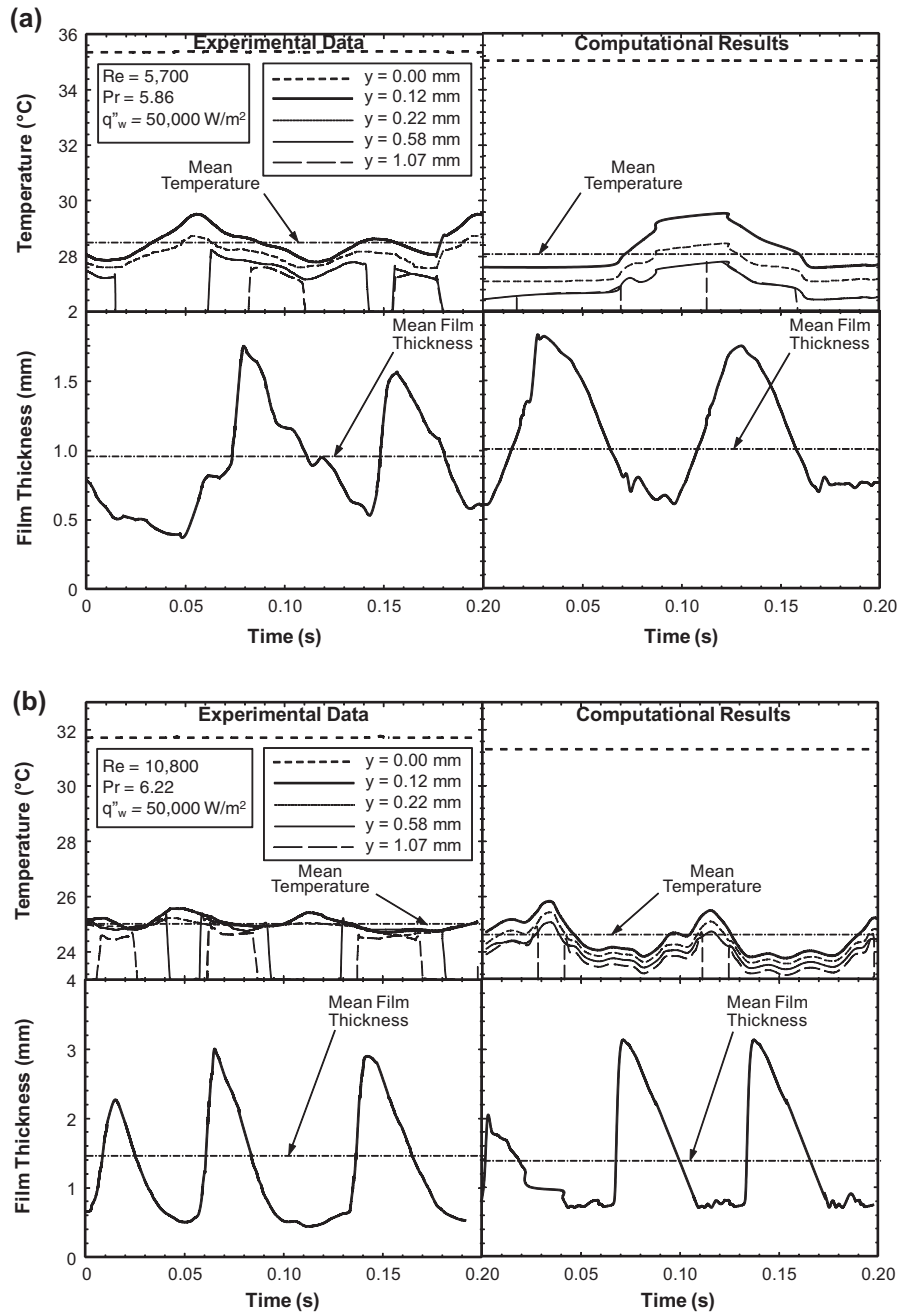All dimensions in mm

Outlet

Fig. 4. Computational domain.

Fig. 5. Comparison of measured and computed time records of film thickness and temperature across the liquid film at $x = 278$ mm for (a) $Re = 5{,}700$, $Pr = 5.86$ and $q''_w = 50{,}000$ W/m^2, and (b) $Re = 10{,}800$, $Pr = 6.22$ and $q''_w = 50{,}000$ W/m^2.

The falling film transport behavior is predicted using the FLU-ENT Analysis System in the Toolbox of ANSYS Workbench 14.0.0 [32]. A toolset labeled Project Schematic in the Workbench interface enables geometry creation, meshing, processing and post-processing. The standard two-equation $\kappa - \varepsilon$ turbulent model included in the ANSYS Guide [32] is used to predict two-dimensional momentum and heat transfer characteristics in the computational domain, with the two-phase treatment following the Volume of Fluid (VOF) Model [33], and solid–liquid interfaces governed by continuities of both temperature and heat flux,

$$T_{s,\Gamma} = T_{f,\Gamma} \qquad (1)$$

and

$$-k_s \frac{\partial T}{\partial r}\bigg|_{\Gamma} = -k_f \frac{\partial T}{\partial r}\bigg|_{\Gamma}. \qquad (2)$$

The governing equations used in the simulation are the Reynolds Averaged Navier Stokes (RANS) equations for unsteady, turbulent and incompressible flow with constant properties. The time-averaged continuity, axial and radial momentum, and energy RANS equations are given, respectively, as [34]

$$\frac{\partial \bar{u}_x}{\partial x} + \frac{1}{r} \frac{\partial (r \bar{u}_r)}{\partial r} = 0, \qquad (3)$$
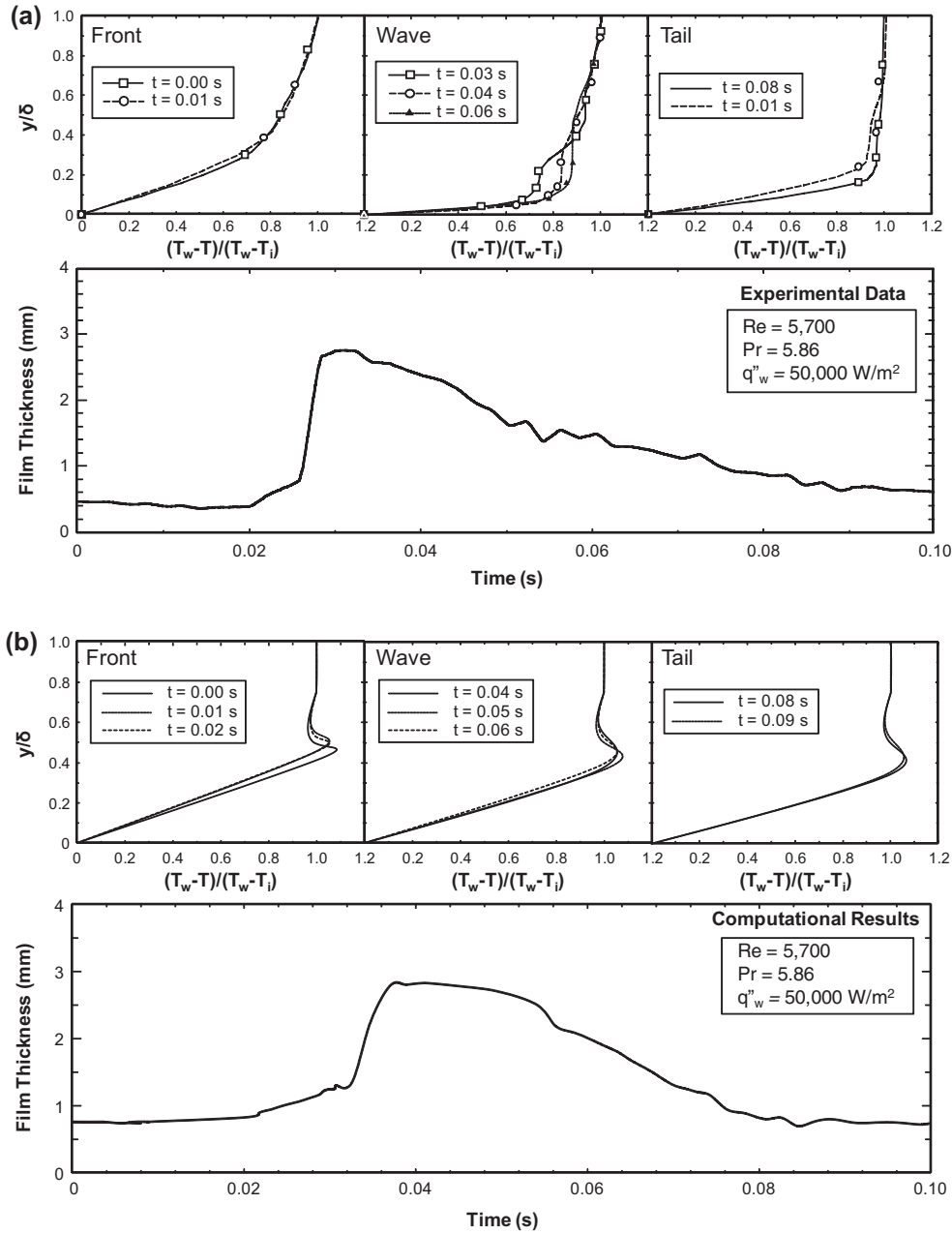
Fig. 6. (a) Measured and (b) computed temperature profiles at different times within the wave period at $x = 278$ mm for $Re = 5,700$, $Pr = 5.86$ and $q''_w = 50,000$ W/m^2.

$$\rho\left(\frac{\partial \bar{u}_x}{\partial t} + \bar{u}_x\frac{\partial \bar{u}_x}{\partial x} + \bar{u}_r\frac{\partial \bar{u}_x}{\partial r}\right) = -\frac{\partial P}{\partial x} + 2\frac{\partial}{\partial x}\left(\mu\frac{\partial \bar{u}_x}{\partial x}\right)$$

$$+ \frac{1}{r}\frac{\partial}{\partial r}\left(r\mu\left(\frac{\partial \bar{u}_x}{\partial r} + \frac{\partial \bar{u}_r}{\partial x}\right)\right)$$

$$- \rho\left\langle \frac{\partial u_x'^2}{\partial x} + \frac{\partial(u_x'u_r')}{\partial r} + \frac{u_x'u_r'}{r}\right\rangle + \rho g, \quad (4)$$

$$\rho\left(\frac{\partial \bar{u}_r}{\partial t} + \bar{u}_x\frac{\partial \bar{u}_r}{\partial x} + \bar{u}_r\frac{\partial \bar{u}_r}{\partial r}\right) = -\frac{\partial P}{\partial r} + \frac{\partial}{\partial x}\left(\mu\left(\frac{\partial \bar{u}_x}{\partial r} + \frac{\partial \bar{u}_r}{\partial x}\right)\right)$$

$$+ 2\frac{1}{r}\frac{\partial}{\partial r}\left(r\mu\frac{\partial \bar{u}_r}{\partial r}\right) - 2\mu\frac{\bar{u}_r}{r^2}$$

$$- \rho\left\langle \frac{\partial(u_x'u_r')}{\partial x} + \frac{\partial u_r'^2}{\partial r} + \frac{u_r'^2}{r}\right\rangle, \quad (5)$$

and

$$\frac{\partial \bar{T}}{\partial t} + \bar{u}_x\frac{\partial \bar{T}}{\partial x} + \bar{u}_r\frac{\partial \bar{T}}{\partial r} = \frac{\partial}{\partial x}\left(\alpha\frac{\partial \bar{T}}{\partial x} - \langle u_x'T'\rangle\right) + \frac{1}{r}\frac{\partial}{\partial r}\left(\alpha r\frac{\partial \bar{T}}{\partial r} - r\langle u_r'T'\rangle\right). \quad (6)$$

The eddy viscosity hypothesis is used to relate the fluctuating terms to the gradient of the mean quantities and the eddy viscosity, where the eddy viscosity, μ_t, is expressed as

$$\mu_t = \frac{C_\mu \rho k^2}{\varepsilon}. \quad (7)$$

The kinetic energy and dissipation energy equations are given, respectively, by

$$2\nabla.\mu\langle \vec{\nabla}s_{ij}\rangle = \frac{\partial}{\partial x}\mu\left\{\frac{\partial k}{\partial x} + \frac{\partial \langle u_x'^2\rangle}{\partial x} + \frac{1}{r}\frac{\partial r\langle u_x'u_r'\rangle}{\partial r}\right\}$$

$$+ \frac{1}{r}\frac{\partial}{\partial r}\mu r\left\{\frac{\partial k}{\partial r} + \frac{\partial \langle u_x'u_r'\rangle}{\partial x} + \frac{1}{r}\frac{\partial r\langle u_r'^2\rangle}{\partial r}\right\} \quad (8)$$
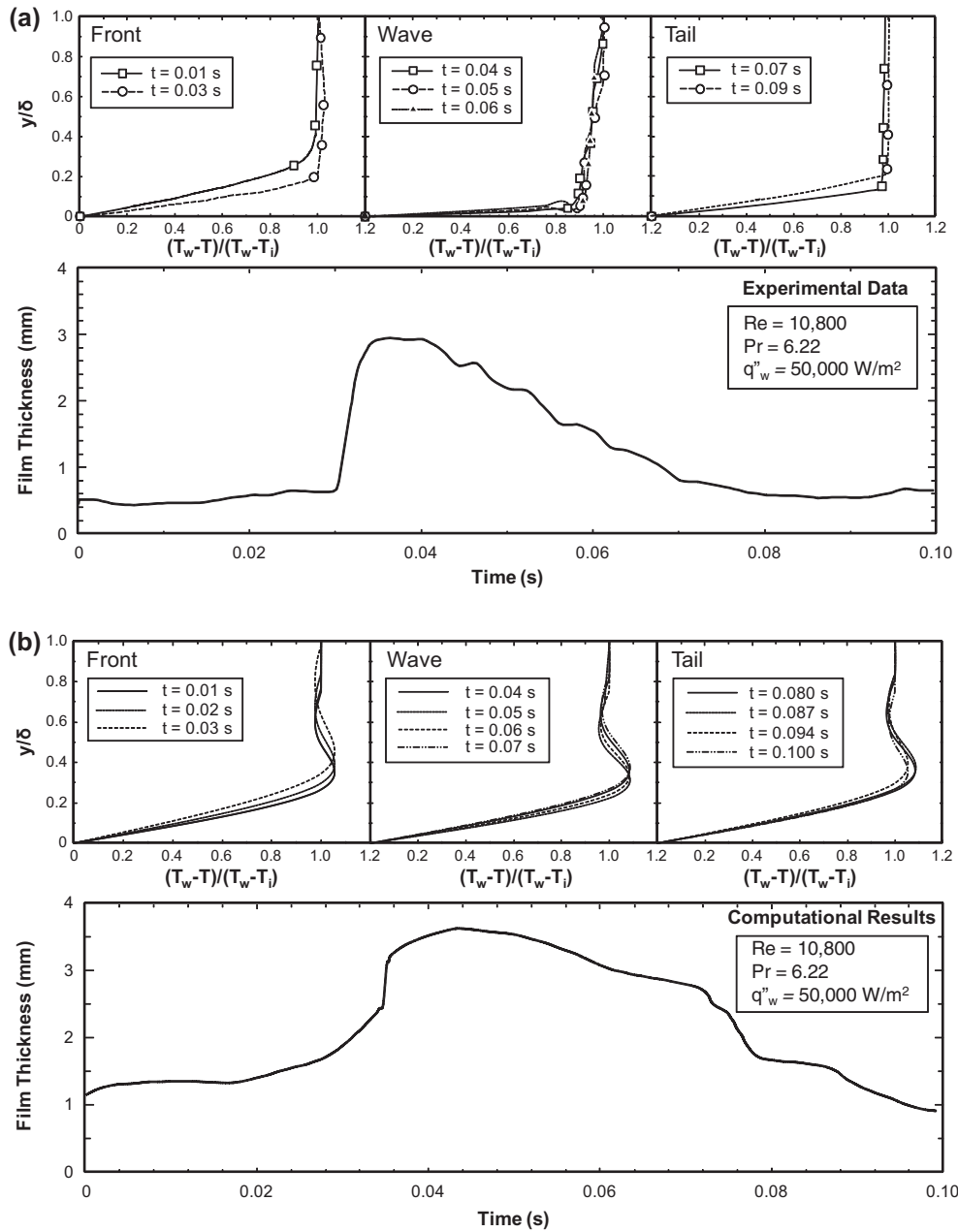
Fig. 7. (a) Measured and (b) computed temperature profiles at different times within the wave period at x = 278 mm for Re = 10,800, Pr = 6.22 and q''_w = 50,000 W/m^2.

and $\quad \varepsilon = \dfrac{2}{\rho}\mu\langle\langle s_{ij}s_{ij}\rangle\rangle,$ \hfill (9)

where $\quad s_{ij} = \dfrac{\partial u'_r}{\partial x} + \dfrac{\partial u'_x}{\partial r}.$ \hfill (10)

A constant turbulent Prandtl number value of $Pr_t = 1$ is used as per [35]. The viscosity-influenced near-wall region is completely resolved all the way to the viscous sublayer. Both e and turbulent viscosity are specified in the near-wall cells. The entire domain is subdivided into a viscosity-influenced region and a fully turbulent region, and demarcation of the two regions is determined by a wall-distance-based turbulent Reynolds number. In the fully turbulent region, the k - e model is employed to define turbulent viscosity. In the viscosity-affected near-wall region, the one-equation model of Wolfstein [36] is employed. In this model, the momentum equations and the k equation are retained. However, the

length scale for turbulent viscosity is derived from Chen and Patel [37]. This two-layer definition for turbulent viscosity is smoothly blended with the high Reynolds number definition from the outer region, as proposed by Jongen [38].

FLUENT combines this two-layer model with a modified formulation of the law of the wall as a single function for the entire wall region by blending laminar and turbulent law of the wall relations as per Kader [39]. This approach allows the fully turbulent relation to be easily modified and extended to take into account other effects such as pressure gradients or variable properties. This formulation also guarantees the correct asymptotic behavior for large and small values of y^+ and reasonable representation of velocity profiles where y^+ falls inside the buffer region.

A numerical method to solving the conjugate heat transfer problem is to treat the solid and fluid as a unitary computational domain and solve the above governing equations simultaneously
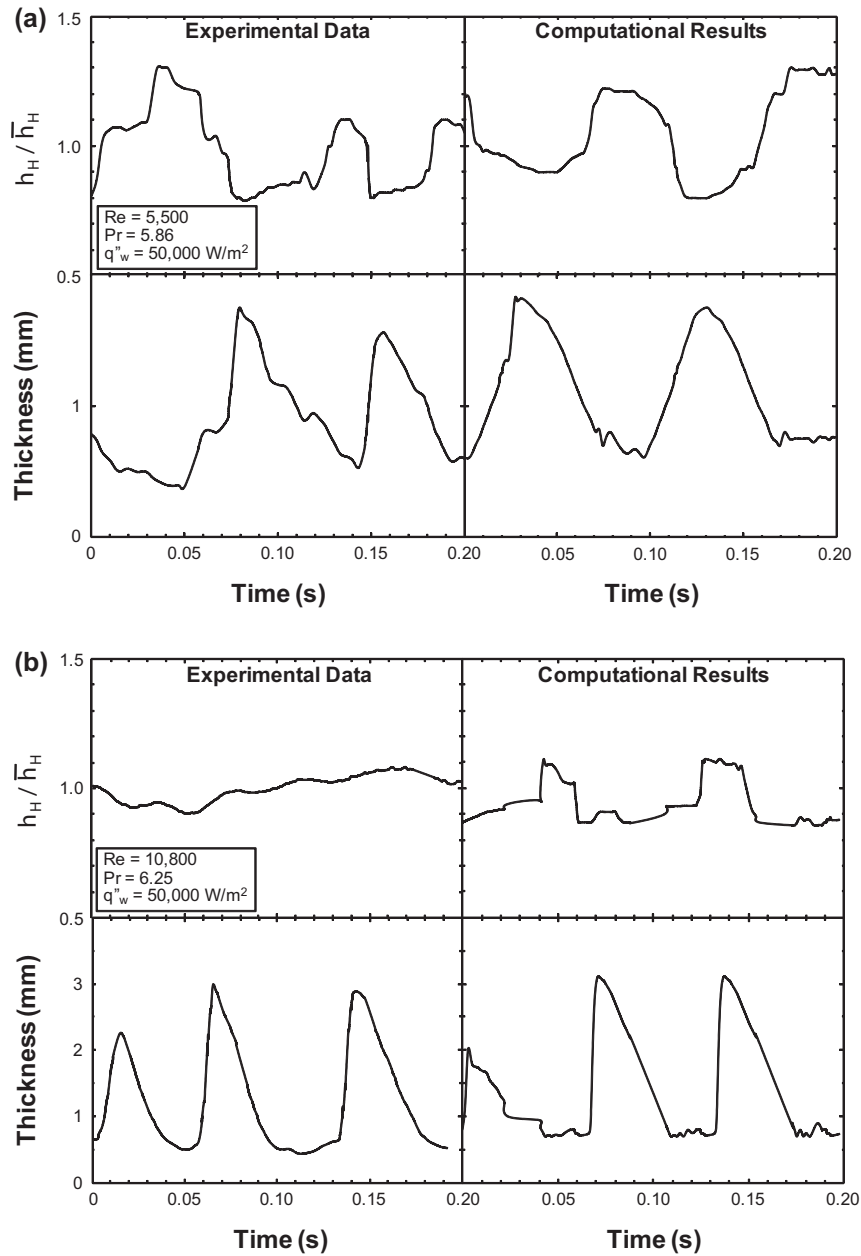
Fig. 8. Comparison of measured and computed time records of film thickness and normalized heat transfer coefficient at $x = 278$ mm for (a) $Re = 5,700$, $Pr = 5.86$ and $q''_w = 50,000$ W/m², and (b) $Re = 10,800$, $Pr = 6.22$ and $q''_w = 50,000$ W/m².

[40]. The boundary conditions are specified in terms of uniform velocity and liquid temperature in the inlet reservoir according to the desired Re and Pr, with $U = vRe/D_H$, $V = 0$, and $T = T_{in}(Pr)$ for $x = -1,060$ mm and -12.7 mm $\leqslant r \leqslant -6.6$ mm. The outlet condition at the bottom of the domain is assumed to be uniform pressure equal to atmospheric pressure to conform to experimental conditions. A constant heat flux is applied along the outer wall of the lower stainless steel portion of the test section; $-k_s \partial T / \partial r = q''_w$ for $0 \leqslant x \leqslant 781$ mm. The porous film distributor has a porosity of 0.002 and a viscous resistance of 3.846×07 m^{-2}. Surface tension effects are considered on all walls by prescribing wall adhesion in terms of contact angle at the walls.

The model considers vapor shear and influences of surface tension and molecular viscosity at the film interface. The tangential and normal force balance equations at the film surface are given, respectively, by

$$e_{i,j} n_j t_i = 0 \tag{11}$$

and

$$-P + 2\mu e_{i,j} n_j t_i = \sigma \left(\frac{1}{R_1} + \frac{1}{R_2} \right). \tag{12}$$

The curvature terms in each cell are calculated by FLUENT from the volume fraction gradients, as per the continuum surface force model proposed by Brackbill et al. [41].

In order to conserve computation time, the fractional step version of the Non-Iterative Time Advancement (NITA) scheme is used with first-order implicit discretization at every time-step [42,43] to obtain pressure-velocity coupling. Gradient generation during spatial discretization is accomplished using the least-squares cell-based scheme [44], while PRESTO, QUICK, Geo-reconstruct and first-order upwind schemes [45] are used for pressure, momentum,
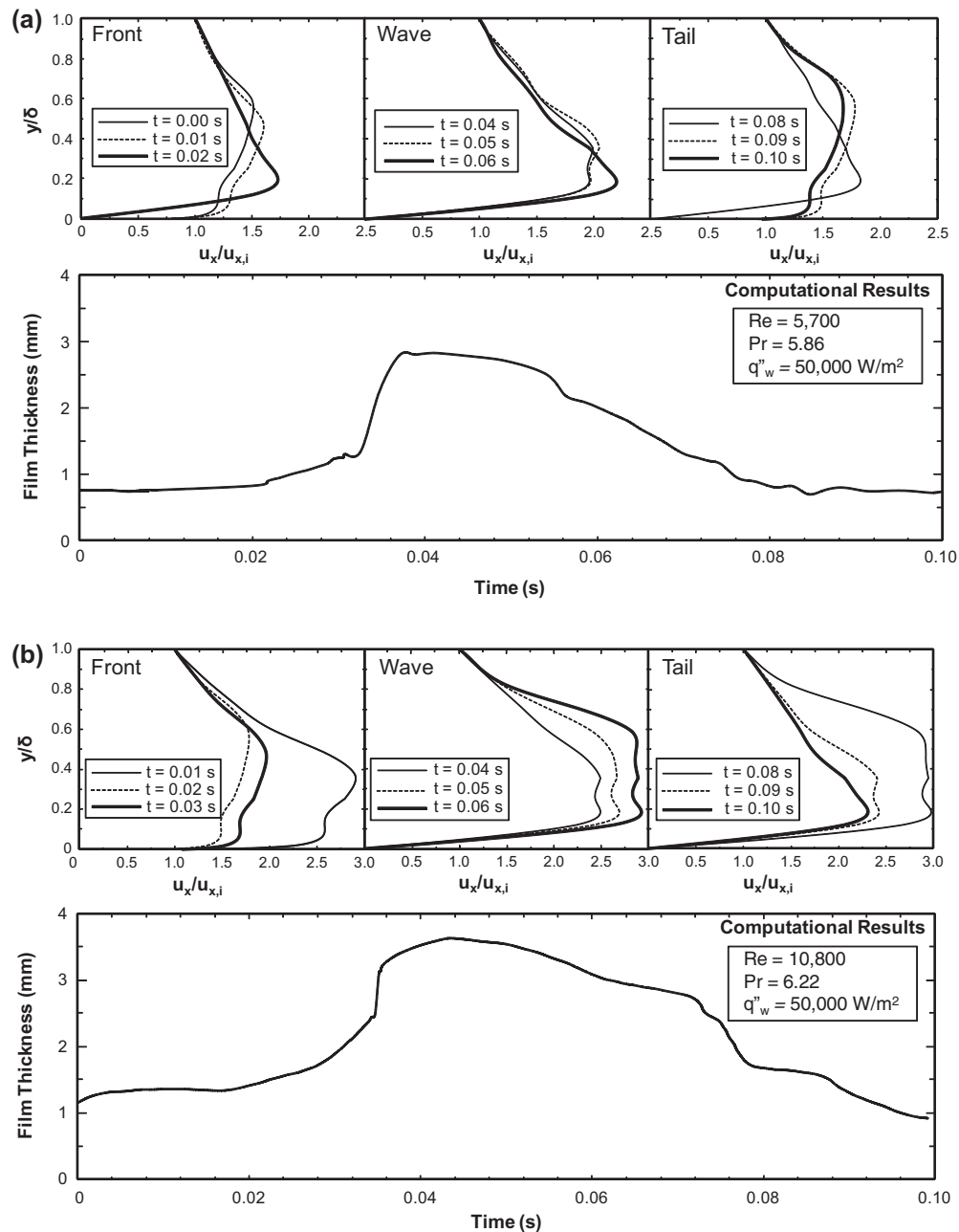
Fig. 9. Computed x-velocity profiles at different times within wave period at x = 278 mm for (a) Re = 5,700, Pr = 5.86 and q''_w = 50,000 W/m^2, and (b) Re = 10,800, Pr = 6.22 and q''_w = 50,000 W/m^2.

volume fraction and turbulent kinetic energy resolution, respectively.

The grid system consists of 401,426 nodes and 397,111 cells, which is arrived at based on careful assessment in pursuit of optimum degree of mesh refinement. This grid is non-uniform, with a larger number of grid points used near the wall, film interface, porous zone and heated portion of the test section to achieve superior accuracy in resolving key flow parameters. Although the bulk flow region of the falling film is modeled using the mesh size recommended for turbulence simulation (>25 cells within 1 $y^+ \times y^+$ grid), an order of magnitude refinement in the mesh is adopted beginning well outside the narrow viscous layer at the interface to ensure high resolution in capturing turbulence at the interface. Care is also taken to ensure that the transition in refinement does not influence the flow.

4. Results

4.1. Thermal characteristics

Unlike the authors' recent study [29], which considered a broad range of film Reynolds numbers, the present computations are performed for two specific turbulent film conditions: (a) Re = 5,700, Pr = 5.86 and q''_w = 50,000 W/m^2, and (b) Re = 10,800, Pr = 6.22 and q''_w = 50,000 W/m^2 that conform to measurements using the multi-probe instrumentation described earlier. The vapor temperature is 25 °C. The simulation is allowed to run until such a time that the film flow is well established and shows consistent temporal and spatial trends. The data discussed here include temperature profile records from [20] and [21].
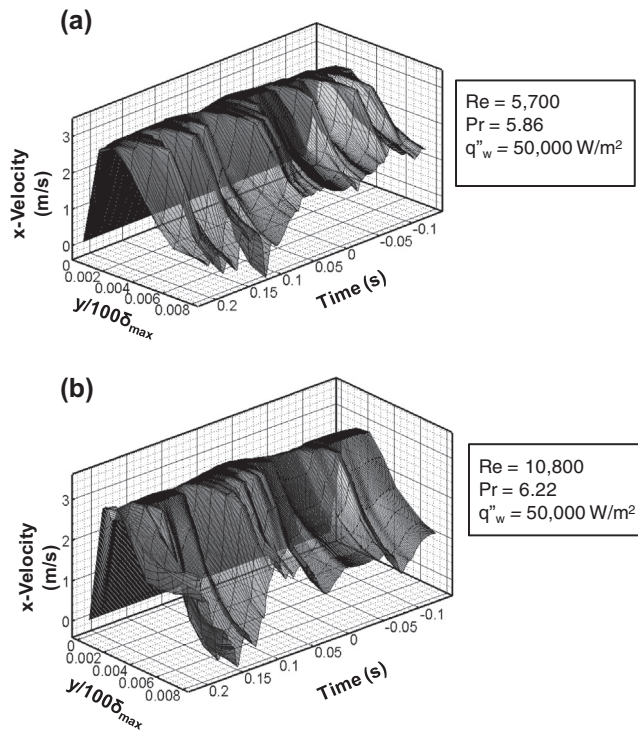
(a)

(b)

Fig. 10. Computed time records of x-velocity component across the liquid film at $x = 278$ mm for (a) $Re = 5,700$, $Pr = 5.86$ and $q''_w = 50,000$ W/m^2, and (b) $Re = 10,800$, $Pr = 6.22$ and $q''_w = 50,000$ W/m^2.

Fig. 5(a) and (b) show time records of liquid temperature measured simultaneously at four distances from the wall ($y = 0.12$, 0.22, 0.58 and 1.07 mm) along with the wall temperature ($y = 0$) measured by the inner wall thermocouple and film thickness for $Re = 5,700$ and 10,800, respectively. The FLUENT predictions are compared with measurements that are performed at $x = 278$ mm. Unlike the wave patterns discussed in [29], the portions of the time record selected here are characterized by waves of larger amplitude, which provide highest resolution in the measured temperature profiles. Notice that the thermocouples at $y = 0.12$ and 0.22 mm are always submerged in liquid, which explains why these records are continuous over time. However, the two thermocouples farther away from the heated wall ($y = 0.58$ and 1.07 mm) show periods of discontinuous drops in temperature because of intermittent exposure to vapor caused by the interfacial waves. As expected, the discontinuity periods increase with increasing distance from the wall. The data show liquid temperature variations that are generally opposite to those of the film thickness: the liquid temperature increases along the thin, substrate portions of the film and decreases within the large waves. This relationship between liquid temperature and thickness is consistent with the findings of Ganchev and Trishin [46].

For $Re = 5,700$, Fig. 5(a) shows that the reverse relationship between temperature and film thickness is fairly consistent across the entire film thickness. The computed results show good agreement with the measured film thickness in terms of mean thickness as well as wave form and period. There is also good agreement between measured and computed wall temperature ($y = 0$) and band of liquid temperatures for the different measurement distances from the heated wall; both the wall and mean film temperatures are predicted within 0.5 °C. The computed results also capture the measured increase in liquid temperature in the film substrate and decrease corresponding to the large waves, albeit with less consistency. It is observed that the reverse relationship between liquid temperature and film thickness is not exact, but rather,

characterized by a phase shift. The points of occurrence of local temperature minima are offset from the wave crest location. Also, there are local temperature peaks in the crest to substrate transition zone. These local excursions will be explained later by examination of the liquid streamlines within the wave.

For $Re = 10,800$, Fig. 5(b) shows measured film thickness records that are similar in shape to those for $Re = 5,700$, but with an increase in both mean thickness and wave amplitude, and a decrease in wave period. These differences reflect the increases in both liquid mass flow rate and liquid velocity with increasing Reynolds number. But compared to $Re = 5,700$, the response of liquid temperatures to the interfacial waves at $Re = 10.800$ is quite attenuated. Two reasons behind this subdued response are (1) the larger thermal mass and larger velocity associated with the thicker substrate between large waves, and (2) intensified mixing due to the more turbulent film flow. Here too, the computed results show good agreement with the measured film thickness in terms of mean thickness as well as wave form and period, with both the wall and mean film temperatures predicted within 0.5 °C. However, the computed temperatures are more reflective of the film thickness variations, and less attenuated than the measured temperatures. This can be attributed to limitations at capturing the attenuation of diffusion effects at higher Reynolds numbers associated with the $\kappa - \varepsilon$ model itself. The computed values do however show significant attenuation when compared to the lower Reynolds number case.

Fig. 6(a) shows, for $Re = 5,700$, measured temperature profiles in three separate regions relative to a large wave: wave front (earlier times), wave itself, and wave tail. The liquid temperature is non-dimensionalized with respect to the difference between wall temperature, T_w, and interface temperature, T_i, and the distance from the wall with respect to film thickness. The data show a steep temperature gradient in the wave compared to the front and tail, however, the gradient in the wave region is exasperated by the larger thickness in this region. Notice for $t = 0.03$ s in the wave region how the temperature profile shows a steep slope near the wall, followed by a short distance where the slope decreases appreciably before increasing once more and ultimately decreasing towards the interface. This behavior is indicative of the complex flow structure in the steep front of the large wave, where the relatively fast moving wave causes liquid from the front to recirculate into the wave. Fig. 6(b) shows computed temperature profiles for a large wave with a thickness profile that resembles the measured profile shown in Fig. 6(a). The computed temperatures in the front, wave and tail regions display similarity in non-dimensional temperature profiles. There are distinct differences from the measured profiles, including a temperature drop in the computed profiles at about $y/\delta = 0.4$, above which the temperature is fairly constant. The temperature drop was observed in [29] as well, and can be attributed to enhanced mixing due to the sharper velocity gradients that exist at this depth, as will be discussed later in conjunction with velocity profile predictions. The temperature drop quickly dissipates away from $y/\delta = 0.4$, as seen in the measurements, but the computations lag in capturing this behavior. Additionally, the computed profiles in the wave region do not reflect the steepness of the measured profiles depicted in Fig. 6(a). This can again be ascribed to the lag in dampening the temperature drop in the computation, although mild steepening of the computed profiles is observed. Fig. 7(a) and (b) show measured and computed temperature profiles, respectively, for $Re = 10,800$. The measured profiles in Fig. 7(a) display trends that are similar to those for $Re = 5,700$, with the wave region showing steeper profiles than the front and tail regions. Fig. 7(b) shows predicted profiles with a noticeable local maximum near $y/\delta = 0.4$, which is not captured in the measured profiles.

Fig. 8(a) and (b) show measured and computed temporal records of the heat transfer coefficient, h_H, for $Re = 5,500$ and
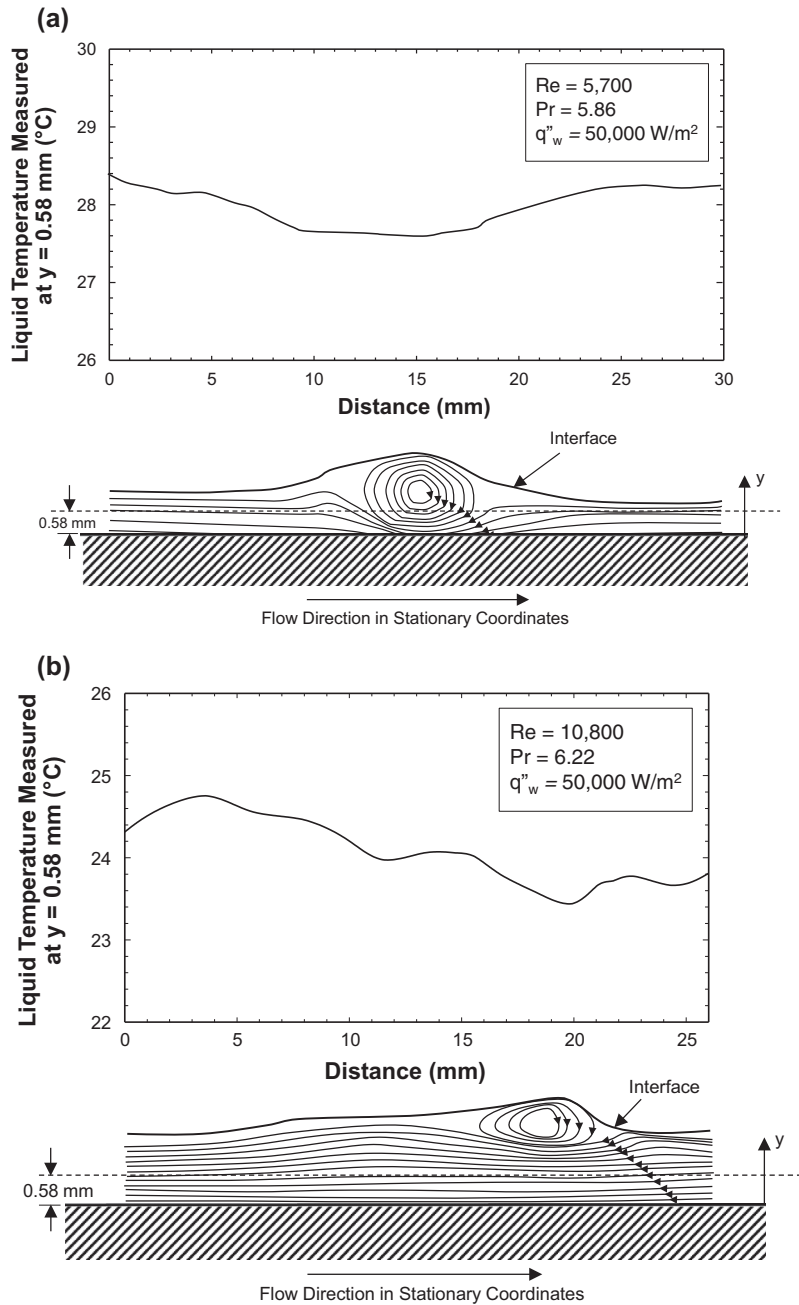
Fig. 11. Computed liquid flow streamlines and liquid temperature measured at $y = 0.58$ mm for (a) $Re = 5,700$, $Pr = 5.86$ and $q''_w = 50,000$ W/m^2, and (b) $Re = 10,800$, $Pr = 6.22$ and $q''_w = 50,000$ W/m^2.

$Re = 10,800$, respectively, where $h_H = q''_w/(T_w - T_m)$, T_m is the mean film temperature, and $\bar{h}_H$ is computed from a relation recently developed by the authors [29],

$$\frac{h_H \nu^{2/3}}{k\, g^{1/3}} = 0.00411 Re^{0.413} Pr^{0.672}. \qquad (13)$$

Equation (13) yields $\bar{h}_H$ values of 6,849 W/m^2.K for $Re = 5,700$, and 7,711 W/m^2.K for $Re = 10,800$. Because q''_w is constant and T_w fairly constant during the passage of large waves, h_H is highest where T_m is highest. Recall how in Fig. 5(a) the time dependence of liquid temperature is opposite to that of film thickness. Fig. 8(a) shows similar time dependence for the heat transfer coefficient that is opposite to that of film thickness. Here too, h_H is highest is the substrate regions upstream and downstream of large waves and lowest in the waves themselves. This trend is reflected

in both the measured and computed temporal records of the heat transfer coefficient. The heat transfer coefficient reaches maximum value in the wave back region, which is consistent with Brauner and Maron's [47] experimental findings concerning mass transfer rate in inclined thin film flows. Fig. 8(b) shows appreciable attenuation in the response of measured h_H to that of film thickness, which is also evident in the measured film temperatures, as discussed earlier in conjunction with Fig. 5(b). And like Fig. 5(b), the computed response of h_H is more reflective of the wave profile, and less attenuated than the measured response.

4.2. Film hydrodynamics

The thermal characteristics discussed so far are strongly influenced by liquid motion within the film, particularly in the

wave region. Fig. 5(a) and (b) show liquid temperature within the relatively cool liquid in the large wave is lowest downstream from the wave crest. This phenomenon is attributed to fluid circulation in the wave as proposed by several investigators [48–50]. Numerical studies by Maron et al. [48] and Wasden and Dukler [49,50] show that the interaction between a large wave and thin substrate causes liquid from the front substrate (*i.e.,* earlier times) to accelerate towards the crest of the large wave. This motion transports high temperature liquid from the substrate to the relatively cold region within the large wave before losing its excess heat due to mixing downstream from the crest. Wasden and Dukler [49] also showed that the velocity gradient is steep and the streamlines close to the wall in the wave's tail region. This provides a plausible explanation why the peak value of the heat transfer coefficient occurs in that region, as shown earlier in Fig. 8(a).

To verify these trends, the velocity field is computed and analyzed for *Re* = 5,700 and 10,800. Fig. 9(a) and (b) show velocity profiles at different times within the front, wave and tail regions of a large wave for *Re* = 5,700 and 10,800, respectively. In theses plots, the *x*-velocity component, u_x, is normalized by the interfacial *x*-velocity, u_i, and the distance from the wall, *y*, by the film thickness, δ. Fig. 9(a) shows the liquid accelerates towards the downstream edge of the front region as it enters the large wave, which is consistent with the findings of Maron et al. [48] and Wasden and Dukler [49,50]. Within the wave region, the velocity possesses a maximum around $y/\delta = 0.3$, and the computed *y*-velocity component (not shown here) peaks near the wave crest. These velocity trends indicate the liquid swirls within the wave region. Notice that the gradient increases in the tail of the wave, which is consistent with the findings of Wasden and Dukler [45], and provides a basis for attaining peak values for the heat transfer coefficient in that region as shown in Fig. 8(a). This is not as apparent in Fig. 8(b), due to the previously mentioned attenuation effects at higher Reynolds number. Notice that the velocity gradient at the interface is not zero, which clearly indicates a finite, albeit weak effect of interfacial vapor shear at the interface.

Fig. 10(a) and (b) show three-dimensional *x*-velocity contour plots for *Re* = 5,700 and 10,800, respectively. Notice how the velocity increases from zero value at the wall to a maximum that is closer to the wall than the interface. There is an increase in velocity in the wave region and acceleration in the wave's upstream portion. The velocity gradients continue to be high in the tail end of the wave. These effects are exasperated at the higher Reynolds number.

Fig. 11(a) and (b) compare liquid streamlines relative to a single large wave for *Re* = 5,700 and 10,800, respectively. These figures also show liquid temperature measured at *y* = 0.58 mm to assess the influence of the wave on liquid temperature. Notice for both Reynolds numbers, that (1) a clear region of liquid recirculation is captured within the large wave, and (2) the liquid flows faster in the larger wave than the upstream and downstream substrates. At *Re* = 5,700, the streamlines are nearly parallel to the wall in the film's substrates. As the large wave overtakes the upstream substrate, the streamlines of upstream liquid move closer to the wall beneath the recirculation zone. Downstream of the wave, the streamlines move away from the wall before subsiding in the downstream substrate to a direction parallel to the wall. In response to these streamline trends, the liquid temperature shows relatively high values both upstream and downstream of the large wave, and a minimum within the wave itself. These trends explain why the heat transfer coefficient is lowest within the large wave. The local temperature maxima and minimum show a finite spatial shift from the upstream substrate-wave and downstream wave-substrate transition zones, and wave crest, respectively. At *Re* = 10,800, the recirculation zone is smaller, and the upstream

and downstream substrates are substantially thicker. Furthermore, the streamlines beneath the recirculation zone are far less influenced by the large wave that at *Re* = 5,700. With the temperature measurement location (*y* = 0.58 mm) falling between streamlines that are fairly parallel to the wall, the liquid temperature response is far more attenuated that at *Re* = 5700.

Overall, the present study demonstrates the effectiveness of computational tools at predicting the hydrodynamic and thermal characteristics of separated flows involving a wavy liquid-vapor interface. It is recommended that future work extend the application of these tools to other types of separated liquid-vapor flows, such those involving heated or condensing liquid films that are shear-driven by fast moving vapor flow. Another important application is transport behavior in flow boiling critical heat flux (CHF), which is preceded by formation of a wavy interface between a liquid core and near-wall vapor layer [51–55].

5. Conclusions

This study examined the influence of interfacial waves on mass, momentum and heat transfer in turbulent, free-falling water films that are subjected to sensible heating. Measurements were presented for two turbulent flow conditions corresponding to *Re* = 5,700 and 10,800. Temporal records of film thickness and temperature profile across the film were used to ascertain the film's thermal response during the passage of large waves. Using FLUENT, a computational model of the falling film was constructed and its predictions compared to the data. Emphasis was placed on the ability of the model to predict the film's response in terms of mean film thickness, wave profile, amplitude and period, wall temperature, mean film temperature, and heat transfer coefficient. Key findings from the study are as follows.

1. The temporal variations of liquid temperature are generally opposite to that of film thickness. The liquid temperature increases in the thin, low thermal mass portions of the film and decreases within the large waves that carry a relatively large portion of the liquid's thermal mass.
2. Increasing *Re* increases the mean thickness and wave amplitude, and decreases the wave period. These trends are attributed to increases in both liquid mass flow rate and liquid velocity with increasing *Re*. However, the higher *Re* causes appreciable attenuation in the measured liquid temperature response to the passage of large waves. This subdued response is the result of larger thermal mass and larger velocity associated with the thicker substrate between large waves, and increased intensity of mixing.
3. The computed results show good agreement with the measured film thickness in terms of mean thickness as well as wave form and period. There is also good agreement between measured and computed wall and mean film temperatures. The computed results capture the measured increase in liquid temperature in the film substrate and decrease corresponding to the large waves. For the higher *Re*, the computed temperatures are more reflective of the film thickness variations, and less attenuated than the measured temperatures.
4. The temporal response of the film's heat transfer coefficient is opposite to that of the film thickness; the heat transfer coefficient is highest is the substrate regions upstream and downstream of large waves and lowest in the waves themselves. Increasing *Re* results in appreciable attenuation in the measured response of the heat transfer coefficient to that of film thickness. The computational results reflect the measured temporal records of the heat transfer coefficient, however, the computed response is less attenuated than the measured for the higher *Re*.

5. Velocity predictions reveal important flow interactions between the film substrate and wave regions. They point to acceleration of high temperature liquid from the upstream substrate toward the cold region within the large wave before losing the excess heat due to mixing downstream from the wave crest.

Acknowledgement

References

[1] L.-T. Yeh, R.C. Chu, Thermal Management of Microelectronic Equipment: Heat Transfer Theory, Analysis Methods, and Design Practices, ASME, New York, 2002.

[2] T.M. Anderson, I. Mudawar, Microelectronic cooling by enhanced pool boiling of a dielectric fluorocarbon liquid, J. Heat Transfer – Trans. ASME 111 (1989) 752–759.

[3] S. Mukherjee, I. Mudawar, Smart pumpless loop for micro-channel electronic cooling using flat and enhanced surfaces, IEEE Trans. – CPMT: Components and Packaging Technologies 26 (2003) 99–109.

[4] S. Mukherjee, I. Mudawar, Pumpless loop for narrow channel and micro-channel boiling from vertical surfaces, J. Electron. Packag. – Trans. ASME 125 (2003) 431–441.

[5] W. Nusselt, Die oberflachenkondensation des wasserdampfes, VDI Zeitschrift 60 (1916) 541–569.

[6] P.L. Kapitza, Collected papers, in: P.L. Kapitza (Ed.), Pergamon Press, New York, 1965.

[7] P. Adomeit, U. Renz, Hydrodynamics of three-dimensional waves in laminar falling films, Int. J. Multiphase Flow 26 (2000) 1183–1208.

[8] K.J. Chu, A.E. Dukler, Statistical characteristics of thin wavy films, AIChE J. 20 (1974) 695–706.

[9] J.R. Bertschy, R.W. Chi, F.W. Abernathy, High-strain-rate free-surface boundary-layer flows, J. Fluid Mech. 126 (1983) 443–461.

[10] A.T. Kirkpatrick, Wave mechanics of inclined and rotating liquid films, Ph.D. Thesis, MIT, Cambridge, MA, 1980.

[11] H. Takahama, S. Kato, Longitudinal flow characteristics of vertically falling liquid films without concurrent gas flow, Int. J. Multiphase Flow 6 (1980) 203–215.

[12] T.D. Karapantsios, S.V. Paras, A.J. Karabelas, Statistical characteristics of free falling films at high Reynolds numbers, Longitudinal characteristics of wavy falling films, Int. J. Multiphase Flow 15 (1989) 1–21.

[13] I. Mudawar, R.A. Houpt, Mass and momentum transport in smooth falling liquid films laminarized at relatively high Reynolds numbers, Int. J. Heat Mass Transfer 36 (1993) 3437–3448.

[14] I. Mudawar, R.A. Houpt, Measurement of mass and momentum transport in wavy-laminar falling liquid films, Int. J. Heat Mass Transfer 36 (1993) 4151–4162.

[15] W. Wilke, Warmeubergang an rieselfilme, VDI Forschungsheft 490 (1962) 1–36.

[16] G. Gimbutis, Heat transfer of a turbulent falling film, in: Proceedings of 5th International Heat Transfer Conference, vol. 2, Tokyo, Japan, 1974, pp. 85–89.

[17] B.G. Ganchev, V.M. Koglov, V.V. Lozovetskiy, Study of heat transfer to a falling fluid film at a vertical surface, Heat Transfer – Sov. Res. 4 (1972) 102–110.

[18] J.A. Shmerler, I. Mudawar, Local heat transfer coefficient in wavy free-falling turbulent liquid films undergoing uniform sensible heating, Int. J. Heat Mass Transfer 31 (1988) 67–77.

[19] J.A. Shmerler, I. Mudawar, Local evaporative heat transfer coefficient in turbulent free-falling liquid films, Int. J. Heat Mass Transfer 31 (1988) 731–742.

[20] T.H. Lyu, I. Mudawar, Statistical investigation of the relationship between interfacial waviness and sensible heat transfer to a falling liquid film, Int. J. Heat Mass Transfer 34 (1991) 1451–1464.

[21] T.H. Lyu, I. Mudawar, Determination of wave-induced fluctuations of wall temperature and convection heat transfer coefficient in the heating of a turbulent falling liquid film, Int. J. Heat Mass Transfer 34 (1991) 2521–2534.

[22] T.H. Lyu, I. Mudawar, Simultaneous measurement of thickness and temperature profile in a wavy liquid film falling freely on a heating wall, Exp. Heat Transfer 4 (1991) 217–233.

[23] F. Gu, C.J. Liu, X.G. Yuan, G.C. Yu, CFD simulation of liquid film flow on inclined plates, Chem. Engrg. Technol. 27 (2004) 1099–1104.

[24] F. Jafar, G. Thorpe, O.F. Turan, Liquid film falling on horizontal circular cylinders, in: Proceedings of 16th Australasian Fluid Mechanics Conference, Brisbane, Australia, 2007, pp. 1193–1199.

[25] J.F. Xu, B.C. Khoo, N.E. Wijeysundera, Mass transfer across the falling film: simulations and experiments, Chem. Eng. Sci. 63 (2008) 2559–2575.

[26] S. Bo, X. Ma, Z. Lan, J. Chen, H. Chen, Numerical simulation on the falling film absorption process in a counter-flow absorber, Chem. Eng. J. 156 (2010) 607–612.

[27] C.-D. Ho, H. Chang, H.-J. Chen, C.-L. Chang, H.-H. Li, Y.-Y. Chang, CFD simulation of the two-phase flow for a falling film microreactor, Int. J. Heat Mass Transfer 54 (2011) 3740–3748.

[28] F. Sun, F. Xu, Y. Gao, Numerical simulation of liquid falling film on horizontal circular tubes, Frontiers Chem. Sci. Eng. 6 (2012) 322–328.

[29] N. Mascarenhas, I. Mudawar, Investigation of eddy diffusivity and heat transfer coefficient for free-falling turbulent liquid films subjected to sensible heating, Int. J. Heat Mass Transfer 64 (2013) 647–660.

[30] W.J. Marsh, I. Mudawar, Predicting the onset of nucleate boiling in wavy free-falling turbulent liquid films, Int. J. Heat Mass Transfer 32 (1989) 361–378.

[31] R. Walraven, Digital filters, in: Proceeding of Digital Equipment Computer Users Society, San Diego, CA, 1980, pp. 827–834.

[32] ANSYS FLUENT 12.1 in Workbench User's Guide. ANSYS Inc., Canonsburg, PA, 2009.

[33] C.W. Hirt, B.D. Nicholls, Volume of fluid (VOF) method for dynamics of free boundaries, J. Comput. Phys. 39 (1981) 201–225.

[34] J.O. Hinze, Turbulence, McGraw-Hill, New York, NY, 1975.

[35] W.M. Kays, Turbulent Prandtl number – where are we?, J Heat Transfer – Trans. ASME 116 (1994) 284–295.

[36] M. Wolfstein, The velocity and temperature distribution of one-dimensional flow with turbulence augmentation and pressure gradient, Int. J. Heat Mass Transfer 12 (1969) 301–318.

[37] H.C. Chen, V.C. Patel, Near-wall turbulence models for complex flows including separation, AIAA J. 26 (1988) 641–648.

[38] T. Jongen, Simulation and modeling of turbulent incompressible flows, Ph.D. Thesis, EPF Lausanne, Lausanne, Switzerland, 1992.

[39] B. Kader, Temperature and concentration profiles in fully turbulent boundary layers, Int. J. Heat Mass Transfer 24 (1981) 1541–1544.

[40] S.V. Patankar, A numerical method for conduction in composite materials, flow in irregular geometries and conjugate heat transfer, in: Proceedings of 3rd International Heat Transfer Conference, vol. 3, Toronto, Canada, 1978, pp. 297–302.

[41] J.U. Brackbill, D.B. Kothe, C. Zemach, A continuum method for modeling surface tension, J. Comput. Phys. 100 (1992) 335–354.

[42] S. Armsfield, R. Street, The fractional-step method for the Navier–Stokes equations on staggered grids: accuracy of three variations, J. Comput. Phys. 153 (1999) 660–665.

[43] H.M. Glaz, J.B. Bell, P. Colella, An analysis of the fractional-step method, J. Comput. Phys. 108 (1993) 51–58.

[44] W. Anderson, D.L. Bonhus, An implicit algorithm for computing turbulent flows on unstructured grids, Comput. Fluids 23 (1994) 1–21.

[45] S.V. Patankar, Numerical Heat Transfer and Fluid Flow, Hemisphere, Washington, DC, 1980.

[46] B.G. Ganchev, V.V. Trishin, Fluctuation of wall temperature in film cooling, Fluid Mech. Sov. Res. 16 (1987) 17–23.

[47] N. Brauner, D.M. Maron, Characteristics of inclined thin films, waviness and the associated mass transfer, Int. J. Heat Mass Transfer 25 (1982) 99–110.

[48] D.M. Maron, N. Brauner, G.F. Hewitt, Flow patterns in wavy thin films: numerical simulation, Int. Commun. Heat Mass Transfer 16 (1989) 655–666.

[49] F.K. Wasden, A.E. Dukler, Insights into the hydrodynamics of free falling wavy films, AIChE J. 35 (1989) 187–195.

[50] F.K. Wasden, A.E. Dukler, Numerical investigation of large wave interactions on free falling films, Int. J. Multiphase Flow 15 (1989) 357–370.

[51] C.O. Cersey, I. Mudawar, Effects of heater length and orientation on the trigger mechanism for near-saturated flow boiling critical heat flux - I. Photographic study and statistical characterization of the near-wall interfacial features, Int. J. Heat Mass Transfer 38 (1995) 629–641.

[52] C.O. Cersey, I. Mudawar, Effects of heater length and orientation on the trigger mechanism for near-saturated flow boiling critical heat flux – II. Critical heat flux model, Int. J. Heat Mass Transfer 38 (1995) 643–654.

[53] J.C. Sturgis, I. Mudawar, Critical heat flux in a long, rectangular channel subjected to onesided heating – I. Flow visualization, Int. J. Heat Mass Transfer 42 (1999) 1835–1847.

[54] J.C. Sturgis, I. Mudawar, Critical heat flux in a long, rectangular channel subjected to onesided heating – II. Analysis of critical heat flux data, Int. J. Heat Mass Transfer 42 (1999) 1849–1862.

[55] H. Zhang, I. Mudawar, M.M. Hasan, Flow boiling CHF in microgravity, Int. J. Heat Mass Transfer 48 (2005) 3107–3118.